Electronic Supplementary Material (ESI) for Journal of Materials Chemistry A.


# Transition Metal–Oxygen Covalency in Perovskite to Dominate Syngas Selectivity for Chemical Looping Partial Oxidation

*Bo Jiang[1,3], Lin Li[1,*], Qian Zhang[1], Jing Ma[1], Haotian Zhang[1], Kewei Yu[1],Zhoufeng Bian[2], Xiaoliang Zhang[1], Xuehu Ma[3], Dawei Tang[1,*]*

1, Key Laboratory of Ocean Energy Utilization and Energy Conservation of Ministry of Education, Dalian University of Technology, Dalian, 116023 Liaoning, P. R. China

2, .Key Laboratory of Energy Thermal Conversion and Control of Ministry of Education, School of Energy and Environment, Southeast University, Nanjing 210096 Jiangsu, P.R. China.

3, State Key Laboratory of Fine Chemicals, Liaoning Key Laboratory of Clean Utilization of Chemical Resources, Institute of Chemical Engineering, Dalian University of Technology, Dalian, 116023 Liaoning, P. R. China

[*] *Lin Li: lilinnd@dlut.edu.cn*

[*] *Dawei Tang: dwtang@dlut.edu.cn*

## 1. *Measurements of distortions of perovskite frame*

The deformation in a $FeO_6$ octahedron was evaluated by the distortion index and calculated by the following equation:[1, 2]

$$\delta = \frac{1}{6}\sum_{i}\left[\frac{(r_i - r)}{r}\right]^2 \quad \text{(S1)}$$

where $r_i$ and $r$ represent the Fe–O bond length and the average Fe–O bond length in a $FeO_6$ octahedron, respectively.

The tilting degree of neighboring $FeO_6$ octahedra was measured by the tilting angle and defined by the following equation:

$$\varphi = \frac{\left\langle Fe - O_{(1)} - Fe \right\rangle + \left\langle Fe - O_{(2)} - Fe \right\rangle}{2} \quad \text{(S2)}$$

where $\left\langle Fe - O_{(1)} - Fe \right\rangle$ and $\left\langle Fe - O_{(2)} - Fe \right\rangle$ represent the two different kinds of angles illustrated in Fig. S2, respectively.

## *2. Relationship of Raman wavenumbers, A-site radii, and tilting angles*

The general relationship between the angle of octahedron tilting and the wavenumber of the vibrational mode of rotation, *e.g.*, $A_g(3)$ and $A_g(5)$, was proposed by Weber *et al.* as follows:

$$\omega^2 = B\left(r_{R,c} - r_R\right): \ \left(180 - \theta\right)^2 \tag{S3}$$

where $B$ is a scaling constant, $r_R$ is the ionic radius of the rare earth, and $r_{R,c}$ is the hypothetical ionic radius for which the octahedra tilting becomes zero.

From Eq. (S3), we can conclude that the smaller the radius of A-site rare earth, the smaller the tilting angle, and therefore the more serious the tilting degree.

### 3. *Relationship between the covalency and oxygen vacancy formation energy*

The oxygen vacancy formation can be expressed by Kröger–Vink notation as follows:

$$2B_B^{\times} + O_O^{\delta} \rightarrow \{B_B' - V_O - B_B'\} + \frac{1}{2}O_2 \quad \text{(S4)}$$

where $O_o^{\delta}$ and $V_o$ represent lattice oxygen and oxygen vacancy sites, respectively, and $B_B^X$ and $B_B^{'}$ refer to the transition metal before and after the formation of an oxygen vacancy. To shed light on the mechanism of oxygen vacancy formation, we decompose the $\Delta E(V)$ into geometrical and electronic contributions as follows:

$$\Delta E(V) = \varepsilon(V) + q\Delta \quad \text{(S5)}$$

where $\varepsilon(V)$ is the energy of forming a randomly distributed and noninteracting oxygen vacancy, and $q\Delta$ is the energy change related with the electron transfer from $O_o^{\delta}$ to remaining $B_B^{'}$ ions. The first term is governed by the oxygen-site Coulombic interactions, *i.e.*, the crystal lattice energy.[3] Hence, Eq. (S5) can approximate to the following equation:

$$\Delta E(V) \approx U_O + q\Delta \quad \text{(S6)}$$

where $U_O$ represents the Madelung potential of oxygen sites and is a function only of the crystal geometry, suggesting that it shares similar values among the spacegroup of *Pnma*. The first term of Eq. (S6) signifies the ionic character of Fe–O bonds, while the latter indicates the covalency of the bonds.

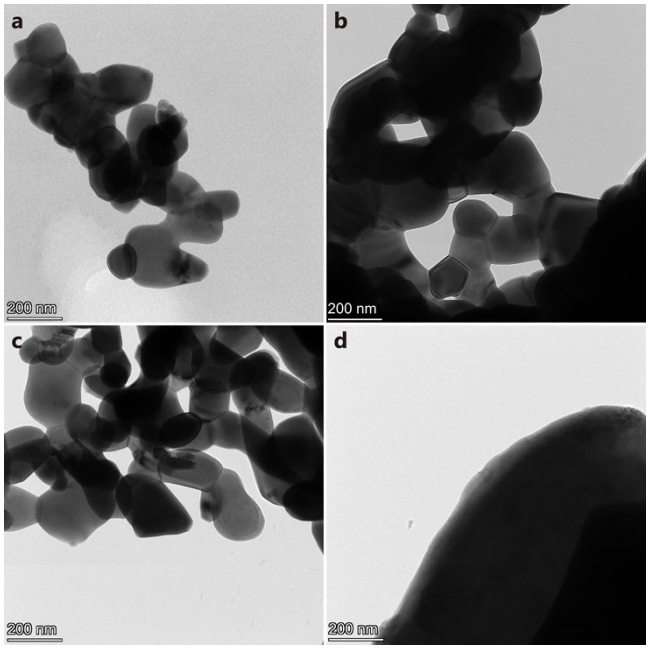


**Figure S1.** TEM images of (a) $LaFeO_3$, (b) $PrFeO_3$, (c) $SmFeO_3$, and (d) $GdFeO_3$.

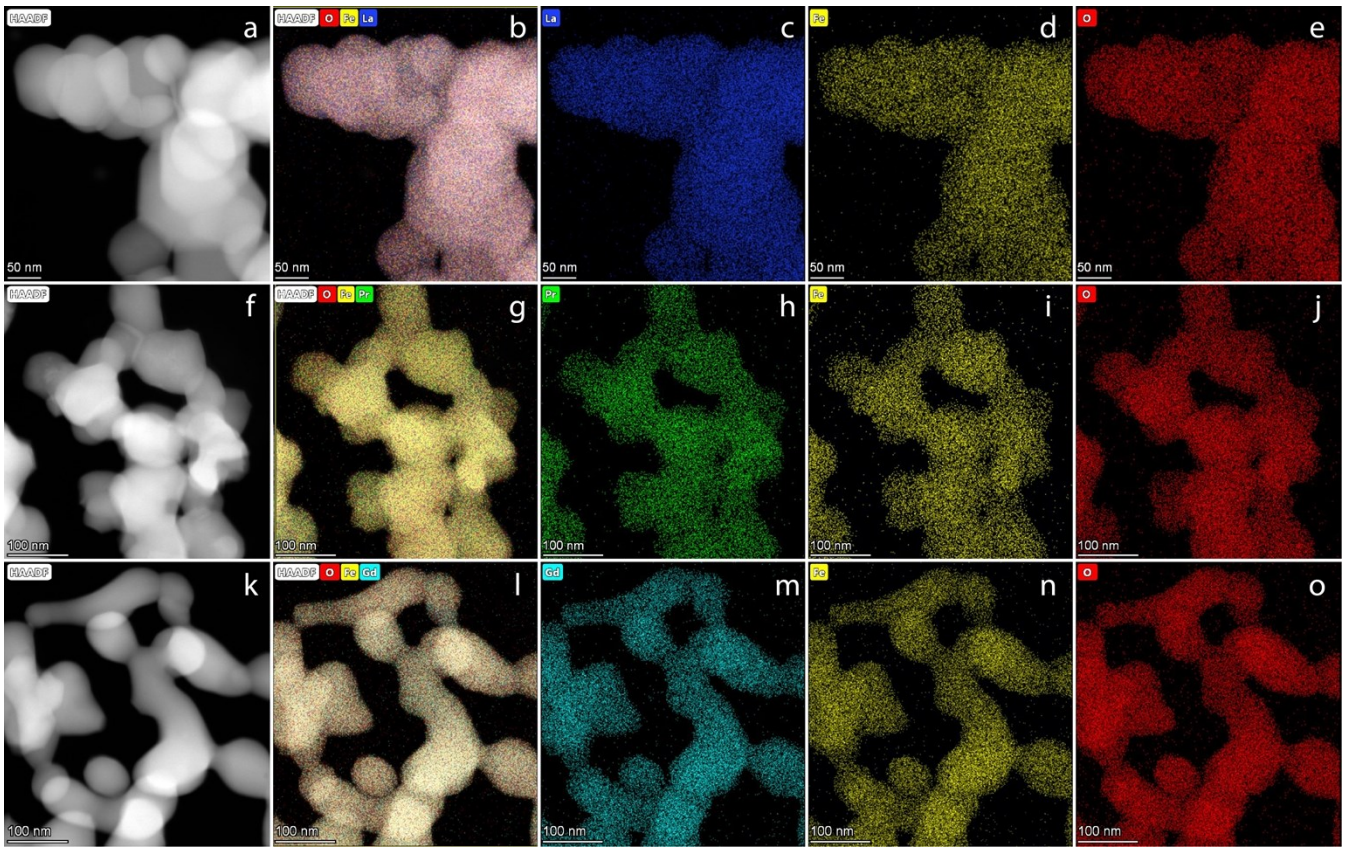


**Figure S2.** HAADF-STEM and element mapping images of $LaFeO_3$ (a–e), $PrFeO_3$ (f–j), and $GdFeO_3$ (k–o).

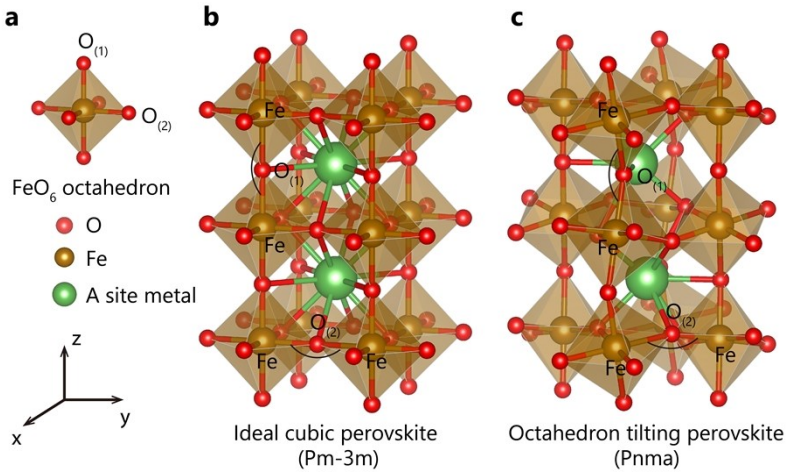


**Figure S3.** Perovskite structures (spacegroup of *Pnma*) and different kinds of Fe–O–Fe bond angles. Oxygen atoms situated at the *z* axe of $FeO_6$ octahedra are termed as $O_{(1)}$, while those located in the *x*–*y* planes are designated as $O_{(2)}$.

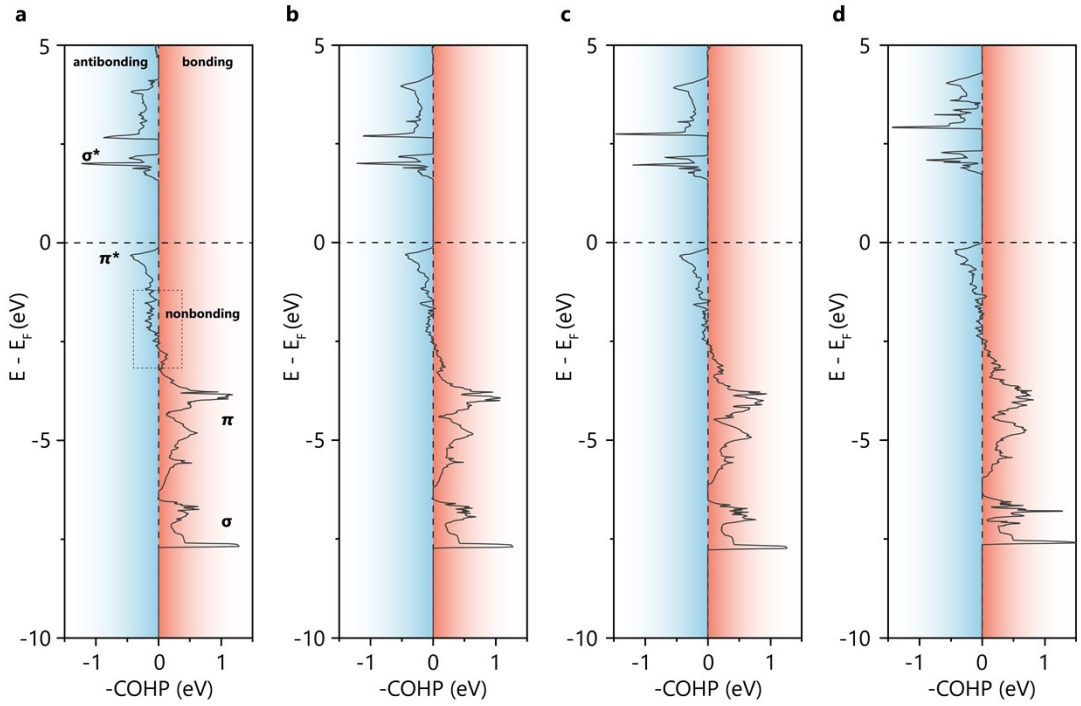


**Figure S4.** Crystal orbital Hamiltonian population for the Fe–O bonds of (a) $LaFeO_3$, (b) $PrFeO_3$, (c) $SmFeO_3$, and (d) $GdFeO_3$.

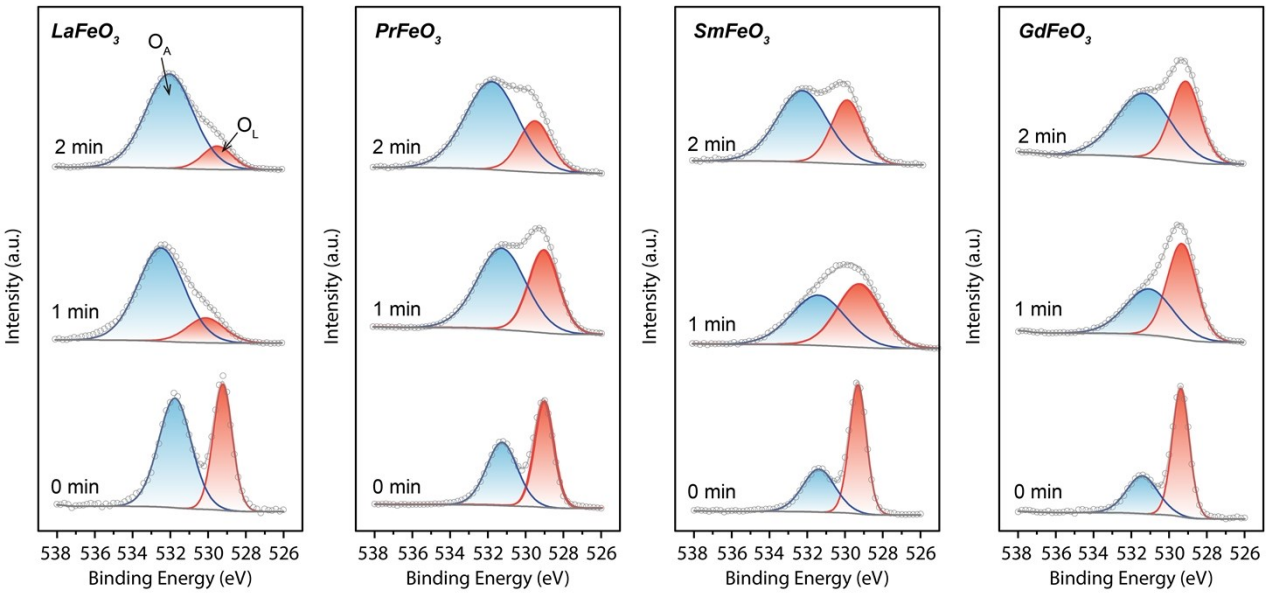


**Figure S5.** *Ex-situ* XPS patterns of $LaFeO_3$, $PrFeO_3$, $SmFeO_3$, and $GdFeO_3$ at the start (0 min), in the middle (1 min), and at the end (2 min) of the reduction step.

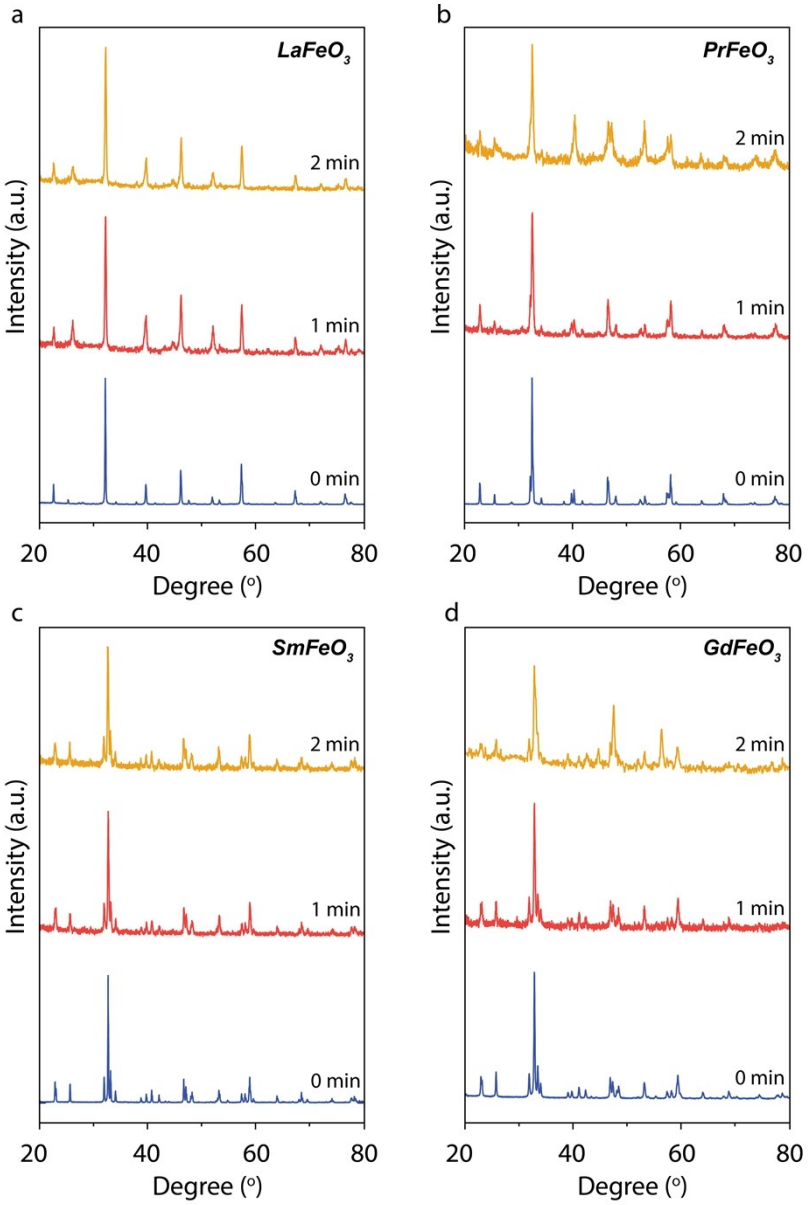


**Figure S6.** *Ex-situ* XRD patterns of $LaFeO_3$, $PrFeO_3$, $SmFeO_3$, and $GdFeO_3$ at the start (0 min), in the middle (1 min), and at the end (2 min) of the reduction step.

**Table S1.** Details of chemicals used in this work.

| Name | Formula | CAS No. | Assay | Company |
|---|---|---|---|---|
| Iron nitrate nonahydrate | $Fe(NO_3)_3•9H_2O$ | 7782-61-8 | 99.99% | Aladdin Reagent (Shanghai) Co., Ltd. |
| Lanthanum nitrate hexahydrate | $La(NO_3)_3•6H_2O$ | 10277-43-7 | 99.99% | |
| Samarium nitrate hexahydrate | $Sm(NO_3)_3•6H_2O$ | 13759-83-6 | 99.99% | |
| Praseodymium nitrate hexahydrate | $Pr(NO_3)_3•6H_2O$ | 15878-77-0 | 99.99% | |
| Gadolinium nitrate hexahydrate | $Gd(NO_3)_3•6H_2O$ | 19598-90-4 | 99.99% | |
| Glycine | $C_2H_5NO_2$ | 56-40-6 | 98.5% | |

**Table S2.** Fe–O bond lengths and Fe–O–Fe bond angles for prepared perovskites obtained from XRD refinement data.

| | | $LaFeO_3$ | $PrFeO_3$ | $SmFeO_3$ | $GdFeO_3$ |
|---|---|---|---|---|---|
| Bond length | $Fe–O_{(1)}$ (Å) | 2.00846 | 2.00163 | 2.00086 | 1.99371 |
| | $Fe–O_{(2)}$ (Å) | 1.98733 | 2.00739 | 2.02596 | 2.03012 |
| | $Fe–O_{(2)}$ (Å) | 2.00194 | 2.01418 | 2.01128 | 2.01643 |
| Bond angle | $Fe–O_{(1)}–Fe$ (°) | 155.451 | 153.069 | 148.690 | 148.130 |
| | $Fe–O_{(2)}–Fe$ (°) | 160.230 | 152.819 | 148.642 | 145.551 |

**Table S3.** Deformation indices and tilting angles of prepared perovskites calculated from Rietveld refinement of XRD data.

| | $LaFeO_3$ | $PrFeO_3$ | $SmFeO_3$ | $GdFeO_3$ |
|---|---|---|---|---|
| Deformation index (δ) | 1.95E-05 | 6.52E-06 | 2.62E-05 | 5.56E-05 |
| Tilting angle (φ) | 157° | 152° | 148° | 146° |

**Table S4.** Crystal radii of Shannon for a coordination number of eight in their trivalent valence states.[5] The tilting of the $FeO_6$ octahedra necessarily induces a distortion of the $AO_{12}$ polyhedra. In the *Pnma* structure, the A cation is usually considered in eight coordination.[6]

| $La^{3+}$ | $Pr^{3+}$ | $Sm^{3+}$ | $Gd^{3+}$ |
|---|---|---|---|
| 130 pm | 127 pm | 122 pm | 119 pm |

**Table S5.** Symmetry assignment and corresponding atomic motions of Raman modes.[7]

| Symmetry | Atomic motion |
|---|---|
| $A_g(1)$ | *R(x)*, in-phase in *x*–*z*, out-of-phase in *y* |
| $A_g(2)$ | *R(z)*, out-of-phase |
| $A_g(3)$ | $[0\ 1\ 0]_{pc}$ $FeO_6$ rotation, in-phase |
| $A_g(4)$ | $O_{(1)}$ *x*–*z* plane |
| $A_g(5)$ | $[1\ 0\ 1]_{pc}$ $FeO_6$ rotation, in-phase |
| $A_g(6)$ | $O_{(1)}$–Fe–$O_{(2)}$ scissor-like bending |
| $B_{2g}(1)$ | *R(x)*, out-of-phase |

**Table S6.** Ratio of adsorbed oxygen species derived from XPS data.

| Reduction time | $LaFeO_3$ | $PrFeO_3$ | $SmFeO_3$ | $GdFeO_3$ |
|---|---|---|---|---|
| 0 min | 0.60 | 0.49 | 0.39 | 0.35 |
| 1 min | 0.83 | 0.61 | 0.49 | 0.59 |
| 2 min | 0.86 | 0.74 | 0.64 | 0.74 |

**REFERENCES**


1. Hirata, T. Oxygen Position, Octahedral Distortion, and Bond-Valence Parameter from Bond Lengths in $Ti_{1-x}Sn_xO_2$ ($0 \leq x \leq 1$). *J. Am. Ceram. Soc.* **2000,** *83*, 3205-3207.

2. Zhang, X.; Pei, C.; Chang, X.; Chen, S.; Liu, R.; Zhao, Z.J.; Mu, R.; Gong, J. $FeO_6$ Octahedral Distortion Activates Lattice Oxygen in Perovskite Ferrite for Methane Partial Oxidation Coupled with $CO_2$ Splitting. *J. Am. Ceram. Soc.* **2020,** *142*, 11540-11549.

3. Sun, Y.; Liao, H.; Wang, J.; Chen, B.;. Sun, S.; Ong, S.J.H.; Xi, S.; Diao, C.; Du, Y.; Wang, J.O. et al. Covalency Competition Dominates the Water Oxidation Structure–Activity Relationship on Spinel Oxides. *Nat. Catal.* **2020,** *3*, 554-563.

4. Janotti, A.; Varley, J.B.; Rinke, P.; Umezawa, N.; Kresse, G.; Van de Walle, C.G. Hybrid Functional Studies of the Oxygen Vacancy in $TiO_2$. *Phys. Rev. B* **2010,** *81*, 085212.

5. Miessler, G.L.; Fischer, P.J.; Tarr, D.A., Inorganic chemistry, fifth ed., Pearson: New Jersey, 2012.

6. Weber, M.C.; Kreisel, J.; Thomas, P.A.; Newton, M.; Sardar, K.; Walton, R.I. Phonon Raman Scattering of $RCrO_3$ Perovskites (R=Y, La, Pr, Sm, Gd, Dy, Ho, Yb, Lu). *Phys. Rev. B* **2012,** *85*, 054303.

7. Weber, M.C.; Guennou, M.; Zhao, H.J.; Íñiguez, J.; Vilarinho, R.; Almeida, A.; Moreira, J.A.; Kreisel, J. Raman Spectroscopy of Rare-Earth Orthoferrites $RFeO_3$ ($R$=La, Sm, Eu, Gd, Tb, Dy). *Phys. Rev. B* **2016**, *94*, 214103.